Epistemic uncertainty quantification of RANS modeling for an underexpanded jet in a supersonic cross flow

By C. Gorlé, M. Emory AND G. Iaccarino

1. Motivation and objectives

The mixing of fuel and air inside supersonic combustion chambers is one of the critical processes for successful operation of scramjet engines and the turbulent mixing models used in Reynolds-averaged Navier-Stokes (RANS) simulations are only a partial representation of the physics. The objective of this work is to develop a novel approach for uncertainty quantification of RANS simulations of turbulent mixing. To achieve this goal, we consider the problem of the mixing of an underexpanded jet in a supersonic cross flow (JISC), because the flow phenomena occurring in this problem are characteristic of the fuel injection and mixing within the combustion chamber of scramjet engines. The typical flow features for this problem are depicted in Figure 1.

Experimental data for an underexpanded sonic air jet injected into a M = 1.6 cross flow of air are reported by Santiago & Dutton (1997). Kawai & Lele (2010) present large-eddy simulation (LES) data for this flow configuration. Another set of experiments is available from Gruber *et al.* (1995, 1996, 1997, 2000) and Lin *et al.* (2010). Hybrid RANS/LES for some of these experiments are reported in Boles *et al.* (2010). Some preliminary simulations for the flow conditions from Lin *et al.* (2010) can be found in Gorlé & Iaccarino (2011). The present paper focuses on the configuration from Santiago & Dutton (1997).

The RANS simulations were performed using the compressible, unstructured finite volume RANS solver JOE (Pecnik *et al.* 2009). The sources of uncertainty in the simulations are the Reynolds stresses in the momentum equations and the scalar fluxes in the scalar transport equations. The Reynolds stress tensor is modeled using the SST k-ω model, whereas the turbulent scalar flux vector is represented using a gradient diffusion model.

In order to quantify the influence of uncertainties in the Reynolds stress tensor and scalar flux vector on the prediction of the quantity of interest, perturbations of the values computed by the models are introduced in the simulations. The Reynolds stresses are perturbed using the methodology described in Emory *et al.* (2011). The perturbations in the scalar flux model are obtained by using the perturbed Reynolds stresses for the calculation of the diffusion coefficient. Initially, a sensitivity study was performed to investigate the influence of the different perturbations. Secondly, the required range of perturbations was determined through a comparison with LES data.

Section 2 describes the flow conditions considered and includes a brief overview of the available experimental and LES data. Section 3 contains more information on the RANS simulations and the different mixing models. The EUQ model is discussed in section 4 and section 5 presents the results. Conclusions and suggestions for future work are presented in section 6.

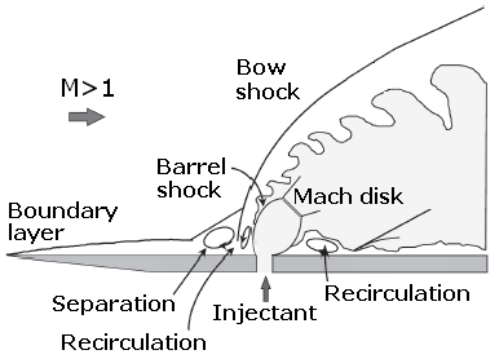

FIGURE 1. JISC flow features (Ben-Yakar *et al.* 2003).

2. Flow conditions and available data sets

2.1. *Flow conditions and experimental data*

The simulations reproduce the conditions of experiments performed by Santiago & Dutton (1997), where an underexpanded sonic air jet is injected into a M = 1.6 cross flow of air. The nozzle has an orifice diameter d of 4.0 mm and the jet to cross flow momentum flux ratio J is equal to 1.7. The total pressure and temperature of the jet are $p_{t,j} = 476$ kPa and $T_{t,j} = 300$ K, for the cross flow $p_{t,\infty} = 241$ kPa and $T_{t,\infty} = 300$ K. The resulting Reynolds number of the jet, based on the nozzle diameter, is 1.1×10^4, the Reynolds number of the cross flow is 1.8×10^5, based on the turbulent boundary thickness of 3.1 mm at the jet orifice.

The experimental data set consists of two-component LDV measurements, conducted both vertically and horizontally at the midline plane and two cross flow planes. The vertical measurements produce the streamwise and wall-normal time-averaged velocity and Reynolds stress components (U, W, $\overline{uu}$, $\overline{ww}$, $\overline{uw}$); the horizontal measurements provide the streamwise and spanwise values (U, V, $\overline{uu}$, $\overline{vv}$, $\overline{uv}$). For the present analysis the focus is on the discrepancy between the Reynolds stress tensor obtained from the RANS simulations and the experiment or the LES, because perturbations will be introduced in the tensor. Since the streamwise Reynolds stress component $\overline{uu}$ is obtained from both the vertical and horizontal LDV measurement, these two data sets can be compared to provide an indication of the accuracy of the experimental values. The comparison revealed a relatively high discrepancy (up to 68% difference in $\overline{uu}/U_{ref}^2$ at measurement locations where the value is large), thereby limiting the use of the measured Reynolds stresses for quantifying the uncertainty in the RANS models.

2.2. *LES data*

LES data sets for a coarse, medium and fine grid are available from Kawai & Lele (2010). The comparison of the time-averaged velocity statistics with the experimental data presented in their paper revealed a good agreement. The scatter obtained when comparing LES and experimental data for the streamwise Reynolds stress component is comparable to the scatter between the horizontal and vertical LDV measurement data. More importantly, a grid dependency study shows a limited dependency of the Reynolds stresses and scalar fluxes on the grid resolution, indicating that the LES results provide a reliable database to quantify the uncertainty in the models for these quantities. Figures

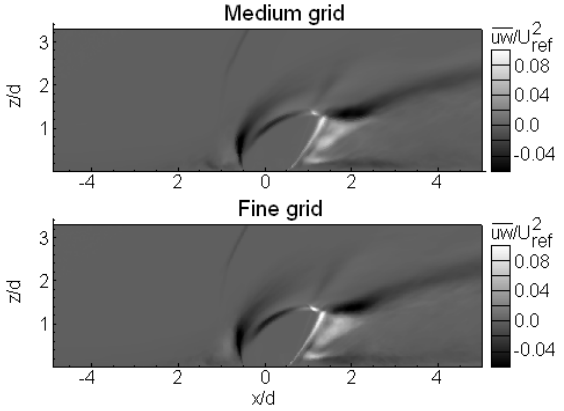

FIGURE 2. Contour of $\overline{uw}/U_{ref}^2$ on the symmetry plane from Kawai & Lele (2010).

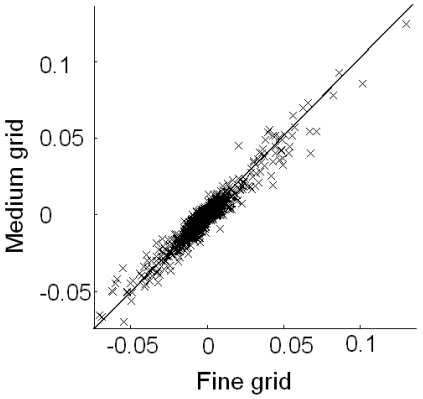

FIGURE 3. Grid dependency of $\overline{uw}/U_{ref}^2$ from Kawai & Lele (2010).

2 and 3 show the non-dimensional Reynolds stress component $\overline{uw}/U_{ref}^2$ obtained using the medium and fine grid and a scatter plot of its value obtained from both grids after interpolation on a uniform Cartesian grid of 8000 points.

3. RANS simulations

The RANS simulations were performed using the JOE flow solver (Pecnik *et al.* 2009). JOE is a compressible, unstructured finite volume Reynolds-averaged Navier-Stokes solver. A second order interpolation of the states is performed at the cell faces, and an HLCC approximate Riemann solver is used for the convective fluxes. All simulations presented used the k-ω SST turbulence model. Details on the boundary conditions and the mesh resolution are presented below. The second subsection introduces the different models considered for the turbulent mixing.

3.1. *Computational model*

The computational domain consists of the nozzle geometry as presented in Figure 4, with the nozzle outlet forming a circular orifice ($d = 4$mm) in a flat plate of size 70×76 mm. The total height of the box into which the jet expands is 36 mm.

At the inlet a turbulent boundary layer profile is prescribed. The experimental boundary layer thickness at the jet orifice is reported as $3.1mm$. The profiles for velocity U, turbulent kinetic energy k and specific dissipation ω were extracted from a 2D simulation to reproduce the reported boundary layer thickness. On the spanwise boundaries the same profiles for U, k and ω are imposed. On the top boundary constant values, matching the profile values at the wall-normal coordinate of the boundary, are prescribed. At the outlet a zero-gradient boundary condition is applied. Because the problem is fully symmetric, only half of the domain was represented. The nozzle and bottom walls are no-slip isothermal walls. At the nozzle inlet, the scalar value is defined as 1, and a uniform velocity that results in sonic conditions at the jet orifice is imposed, in combination with the static pressure and temperature to match the total pressure and temperature from the experiment. The resulting Reynolds number, pressure ratio, and density ratio match those of the experiment.

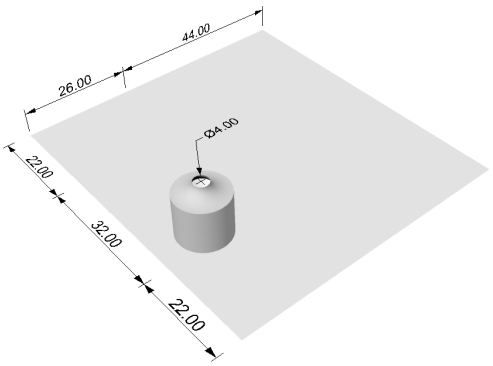

FIGURE 4. Nozzle and dimensions of the computational domain [mm]

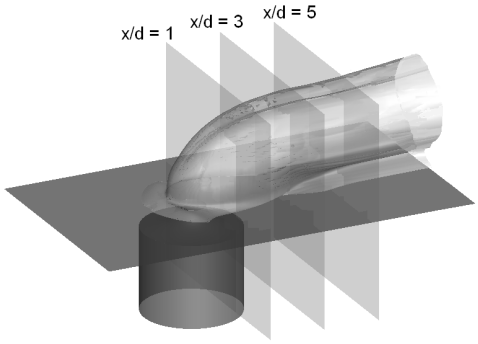

FIGURE 5. Quantity of interest: isolines of scalar value $\phi = 0.028$ extracted from the isosurface at three downstream locations: $x/d = 1$, $x/d = 3$ and $x/d = 5$.

The computational grid consists of 1.5 million hexahedral elements. The cell size on the edge of the jet orifice is 0.1 mm and the resolution on the flat plate decreases away from the nozzle to a maximum cell size of 0.5 mm within the region of interest. The resulting mesh on the flat plate is extruded upward with an initial cell size of 0.001 mm, corresponding to $y^+ \approx 1$ and a maximum of 1.2 mm at the top of the domain. A grid dependency study was performed using a grid of 3.3 million hexahedral elements, which corresponds to an increase in resolution by a factor 1.5 within the region of interest, and no noticeable influence on the flow or scalar field was observed.

The quantity of interest that will be considered is the location of the isolines of the scalar value $\phi = 0.028$ at three downstream locations. Figure 5 illustrates the downstream locations at which the isolines are extracted from the isosurface.

3.2. *Scalar flux models*

Three different formulations for the turbulent diffusion coefficient tensor were considered: the standard gradient diffusion hypothesis, the generalized gradient diffusion hypothesis (Daly & Harlow 2010) and the high-order gradient diffusion hypothesis (Abe & Suga 2001). The standard gradient diffusion hypothesis (SGDH) is the most common approach for modeling the scalar fluxes $\overline{u_i\phi}$ in RANS simulations:

$$\overline{u_i\phi} \approx -\frac{\nu_t}{Sc_t}\frac{\partial\overline{\Phi}}{\partial x_i}, \tag{3.1}$$

where $\overline{\Phi}$ and ϕ are the time-averaged and fluctuating scalar, $\nu_t = \frac{k}{\omega}$ is the turbulent viscosity and Sc_t is the turbulent Schmidt number. Obvious limitations of this model are the assumptions that the diffusion coefficient is isotropic and that it can be defined as the ratio of ν_t and a constant Sc_t. The invalidity of this assumption for modeling the mixing of a jet in a supersonic cross flow is clearly demonstrated in Boles *et al.* (2010), where a local calculation of the turbulent Schmidt number based on results obtained from a hybrid RANS/LES model revealed a large scatter of the values within the flow field.

A first generalization of the SGDH model are the gradient diffusion models which assume a tensorial, anisotropic value of the diffusion coefficient to approximate the scalar

fluxes:

$$\overline{u_i\phi} \approx -D_{t,ij}\frac{\partial\overline{\Phi}}{\partial x_j}. \tag{3.2}$$

Two different formulations for the turbulent diffusion coefficient tensor are considered. The first is the generalized gradient diffusion hypothesis (GGDH, Daly & Harlow 2010):

$$D_{t,ij} = \alpha_{\phi,GGDH}\tau_\phi\overline{u_iu_j}. \tag{3.3}$$

The second is the high-order generalized gradient diffusion hypothesis (HGGDH, Abe & Suga 2001):

$$D_{t,ij} = \frac{\alpha_{\phi,HGGDH}\tau_\phi}{k}\overline{u_iu_k}\;\overline{u_ku_j}. \tag{3.4}$$

α_ϕ is a model constant, τ_ϕ is a time scale equal to $1/C_\mu\omega$ and $\overline{u_iu_j}$ are the components of the Reynolds stress tensor.

The effect of α_ϕ in these models is equivalent to that of Sc_t in the SGDH model. Hence, when comparing the different models, the specification of these model constants should be equivalent. A relationship between the different constants can be derived by considering the case of isotropic turbulence, for which all the models reduce to

$$\overline{u_i\phi} = -C\frac{k}{\omega}\frac{\partial\overline{\Phi}}{\partial x_i}, \tag{3.5}$$

with

$$C_{SGDH} = \frac{1}{Sc_t}\;;\; C_{GGDH} = \frac{2}{3}\frac{\alpha_\phi}{C_\mu}\;;\; C_{HGGDH} = \frac{4}{9}\frac{\alpha_\phi}{C_\mu}. \tag{3.6}$$

Hence, the time scale constants in the generalized models can be reformulated in terms of Sc_t:

$$\alpha_{\phi,GGDH} = \frac{3}{2}\frac{C_\mu}{Sc_t}\;;\; \alpha_{\phi,HGGDH} = \frac{9}{4}\frac{C_\mu}{Sc_t}. \tag{3.7}$$

A comparison of the results obtained using all three models is presented in Section 5.1.

4. EUQ model

As stated before, the most common approach for modeling turbulent mixing in RANS simulations is to use the standard gradient diffusion hypothesis. The sensitivity of the model outcome to the turbulent Schmidt number is significant and performing a parametric study is the most straightforward method to quantify the influence of its value on the prediction. This, however, does not address all sources of uncertainty in the simulations, since such studies are still limited by the assumptions inherent to the model form.

This limitation can be overcome by considering the fundamental sources of uncertainty in the computations. In RANS simulations these are the Reynolds stresses in the momentum equations and the scalar fluxes in the transport equation for the scalar, which both require modeling. To correctly quantify the uncertainty in the simulation outcome, perturbations can be introduced into the values obtained from their models. In the following subsection the methodology for introducing perturbations in the Reynolds stress tensor as developed in Emory *et al.* (2011) is summarized. It consists of decomposing the tensor, typically represented as a random matrix, into a set of uncorrelated stochastic variables. In addition to independent variations of the turbulent stresses, these new random variables provide a unique physical interpretation of the uncertainty being introduced. In the

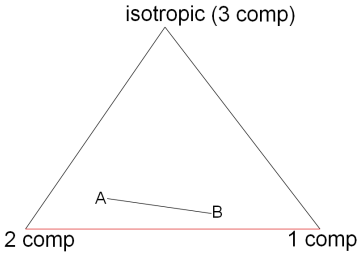

FIGURE 6. Barycentric map.

second subsection, the application of this methodology for perturbing the scalar fluxes is outlined.

4.1. *Introducing uncertainty in the Reynolds stress tensor*

The method described in Emory *et al.* (2011) is based on reformulating the Boussinesq hypothesis $\overline{u_i u_j} \approx (2/3)k\delta_{ij} - 2\nu_t S_{ij}$ in terms of the eigenvalue decomposition of the normalized anisotropy tensor $a_{ij} = \overline{u_i u_j}/(2k) - \delta_{ij}/3 = -(\nu_t/k)S_{ij}$, $\left(a_{ij} - \lambda^{(i)}\delta_{ij}\right) v_j = 0$:

$$\overline{u_i u_j} \approx 2k\left(v_i \lambda^{(i)} v_j + \frac{\delta_{ij}}{3}\right). \tag{4.1}$$

Subsequently, epistemic uncertainty can be introduced in this relation as

$$\overline{u_i u_j} \equiv 2\left(k + \Delta_k\right)\left(\left(v_i + \Delta_{v_i}\right)\left(\lambda^{(i)} + \Delta_{\lambda^{(i)}}\right)\left(v_j + \Delta_{v_j}\right) + \frac{\delta_{ij}}{3}\right). \tag{4.2}$$

At present it is assumed that $\Delta_{v_i} = 0$, and uncertainty is introduced through $\Delta_{\lambda^{(i)}}$ and Δ_k.

The perturbation of the eigenvalues of the Reynolds stress anisotropy tensor is based on modifying the location of the Reynolds stress within the barycentric map proposed in Banerjee *et al.* (2007). The corners of the map represent different limiting states of turbulence anisotropy, and are referred to by their corresponding number of components. Any anisotropy tensor can be represented as a convex combination of these limiting states. The unique location within the map is determined by the coefficient values for this combination, which are functions of λ_i. Figure 6 depicts the barycentric map, which contains all the realizable states of the Reynolds stress tensor.

First the map location of the Reynolds stress computed by the k-ω SST turbulence model is determined from λ_i, then uncertainty is injected by moving it to a new location. Once the new location has been determined, an updated set of eigenvalues corresponding to $(\lambda_i + \Delta_{\lambda^{(i)}})$ is evaluated and used to reconstruct a_{ij} and the Reynolds stress tensor. For the initial sensitivity analysis, the eigenvalues are modified by moving every point all the way to the three corners of the barycentric map. In a second phase, the perturbation is defined from a comparison with the LES data.

The turbulent kinetic energy does not have a realizable upper bound, which makes the definition of the perturbation range less straightforward. For the sensitivity analysis, the original value of k obtained from the k-ω SST model is multiplied or divided by two. In a second phase, the perturbation is defined from a comparison with the LES data.

4.2. *Introducing uncertainty in the scalar flux vector*

Considering the gradient diffusion models with a tensorial diffusion coefficient, a general expression for the scalar flux is given by Eq. 3.2 with:

$$D_{t,ij} \approx C_\phi G\left(u_i u_j\right). \tag{4.3}$$

The uncertainties in this relationship are induced by the value of the model constant C_ϕ and the values for the different components of the Reynolds stress tensor that are used for calculating the function $G\left(u_i u_j\right)$.

Epistemic uncertainty can be introduced into Eq. 4.3 to investigate the sensitivity of the model outcome:

$$\overline{u_i \phi} \equiv -\left(C_\phi + \Delta_{C_\phi}\right) G\left(u_i u_j + \Delta_{u_i u_j}\right) \frac{\partial \overline{\Phi}}{\partial x_j}. \tag{4.4}$$

The sensitivity to both sources of uncertainty has been considered separately. First a variation of C_ϕ, which is equivalent to varying Sc_t in the SGDH model, is performed. Second, the values of the Reynolds stress components used to calculate $G\left(u_i u_j\right)$ are perturbed according to the method summarized in the previous subsection.

For the simulations presented in section 5, the formulation of the GGDH was used for $G\left(u_i u_j\right)$. It is noted that in order to address the full model form uncertainty, Δ_{C_ϕ} should be defined as a spatially varying function for the different scalar flux components. This extension of the approach is the subject of future work, where a comparison of the scalar flux vectors obtained from the RANS and LES will be considered.

4.3. *Range of perturbations from comparison with LES*

To determine the range of perturbations that should be considered for $\Delta_{\lambda^{(i)}}$ and Δ_k, the RANS and LES solution were both interpolated on a Cartesian grid with resolution 0.2d, covering the area between $-5 \leq x/d \leq 5$, $0 \leq y/d \leq 2$, $0 \leq z/d \leq 3.4$.

4.3.1. *Comparison of the eigenvalues*

Figure 7 shows the Barycentric map for the RANS and LES, respectively. The difference between the locations is quantified in terms of the distance D and the angle θ as indicated in the plot. The points in the maps are shaded by the angle of the displacement.

From a detailed analysis, it was found that a distinction can be made between the points where the turbulent production is larger than the turbulent dissipation ($P-\epsilon > 0$) and the points where $P-\epsilon < 0$. In the RANS, the points where $P-\epsilon$ is large tend to be located more toward the one- and two-component corners of the map, whereas for the LES all points are clustered around the center of the map.

On the basis of this comparison the perturbation was defined to first correct this bias by moving all the points to the average location in the LES map, which is indicated as the black dot in Figure 7. Subsequently the location was varied within the circle with radius 0.225. The distribution of the distance from the points in the LES map to the center point is shown in Figure 8, and the radius of the circle was defined as the distance for which the cumulative probability function is equal to 0.9. At present a spatially uniform perturbation was considered.

4.3.2. *Comparison of the turbulent kinetic energy*

Figure 9 presents a comparison of the turbulent kinetic energy from the LES and RANS, including the relative and absolute difference. In regions of relatively high turbulent kinetic energy the relative difference is between 0 and 2. In regions of lower turbulent

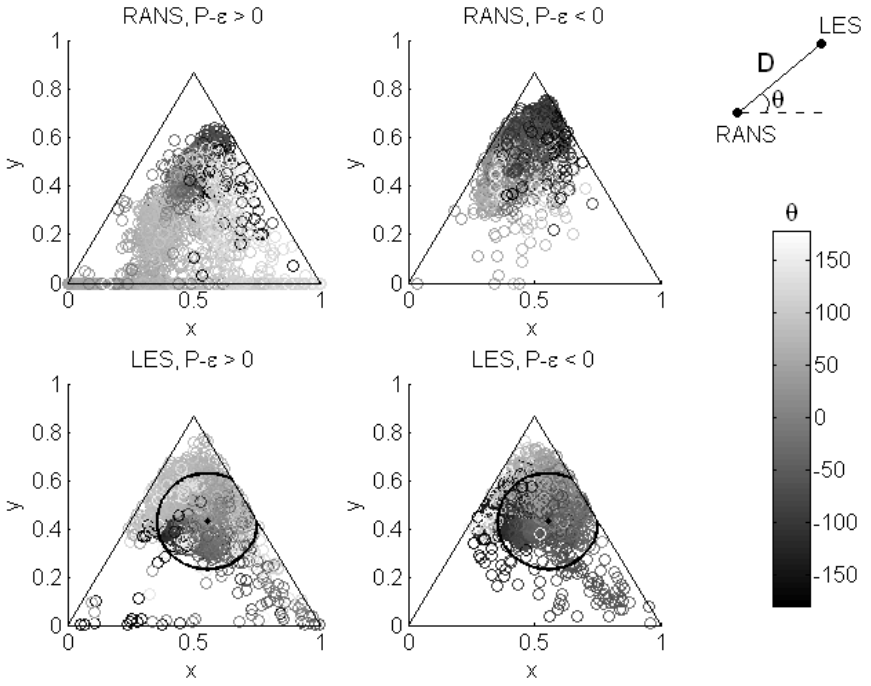

FIGURE 7. Comparison of Barycentric map from RANS and LES.

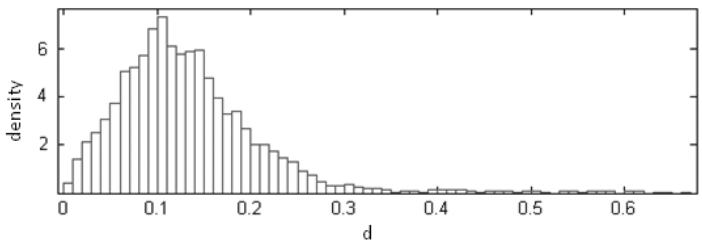

FIGURE 8. Distribution of the distance between the points in the LES map and the average location.

kinetic energy the relative difference does not provide a good measure of the discrepancy, hence the absolute difference is considered. It is obvious that a uniform perturbation (either in relative or in absolute terms) can not represent the differences observed and a spatial variation should be considered.

Consequently, the data was analyzed to define one or more markers that allow the identification of flow regions in which to apply a different perturbation. As for the Barycentric map coordinates, it was found that there is a distinction in the behavior between $P-\epsilon > 0$ and $P - \epsilon < 0$. The latter shows larger differences with the LES, especially in regions of small k. Based on this comparison, the perturbation function for k was defined as indicated in Figure 10. The amplitudes A1 to A3 were varied within a range obtained from the distributions of the difference in k in the three regions. The distributions for the

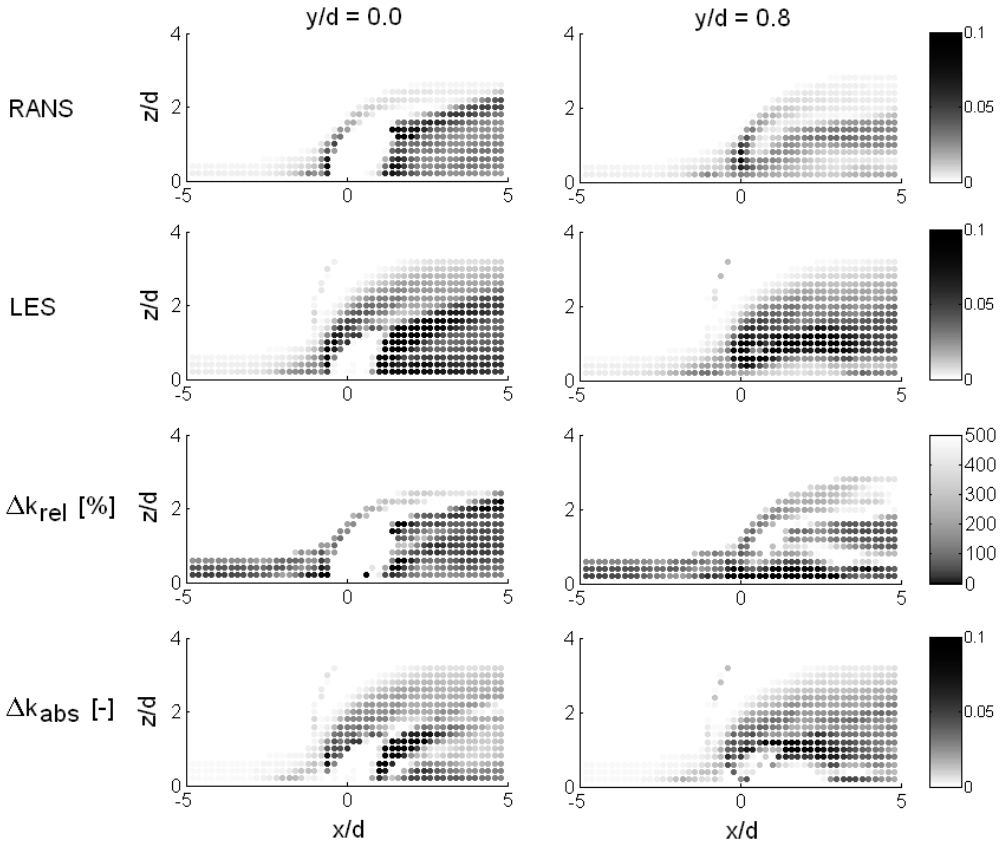

FIGURE 9. Comparison of non-dimensional turbulent kinetic energy k/U_{ref}^2 from LES and RANS, including the relative and absolute difference. The interpolated values on the Cartesian grid nodes are shown at two spanwise locations.

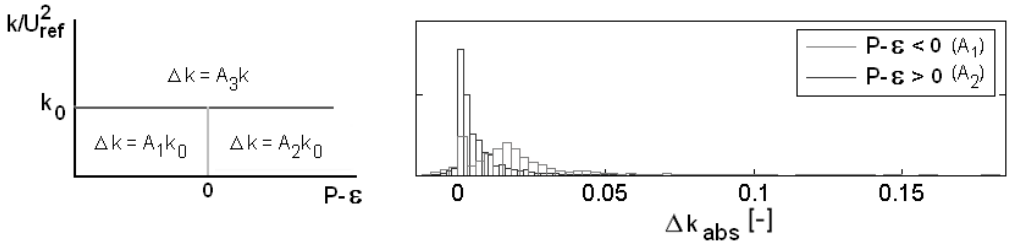

FIGURE 10. Perturbation of k as a function of $P-\epsilon$ and k/U_{ref}^2 (left); distribution of absolute differences between non-dimensional turbulent kinetic energy k/U_{ref}^2 from LES and RANS for $k < k_0$ (right).

regions where k is small are also included in the plot to visualize the different behavior for $P-\epsilon > 0$ and $P-\epsilon < 0$.

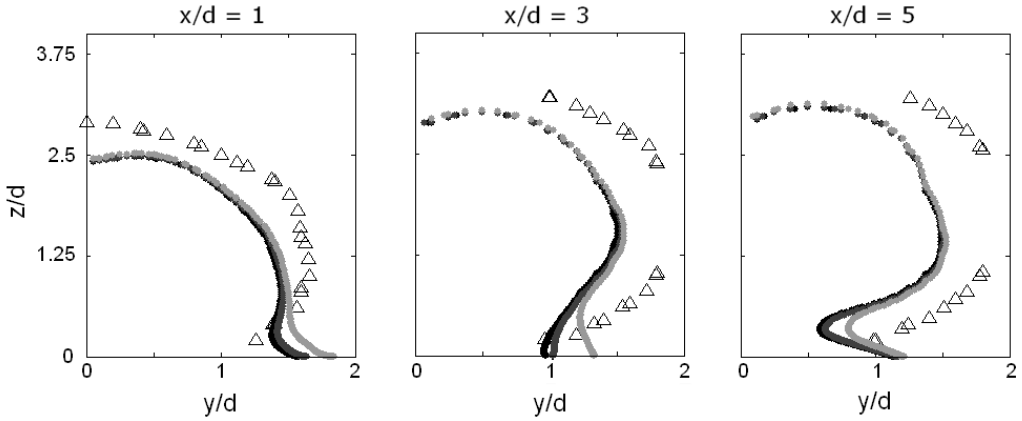

FIGURE 11. Comparison of isolines for $\phi = 0.028$ at three downstream transverse planes: LES (△), SGDH (•), GGDH (•) and HGGDH (•).

5. Results

The results were post-processed by extracting the isolines of the scalar value $\phi = 0.028$ at three downstream locations (Figure 5). In the first subsection, the three different scalar flux models are compared, the second subsection presents the results of a sensitivity analysis that was performed to investigate whether all perturbations affect the mixing and the last subsection presents the results of a preliminary EUQ analysis with the perturbation functions based on the LES/RANS comparison.

5.1. *Comparison of RANS mixing models*

Figure 11 presents a comparison of the isolines obtained with the SGDH, GGDH, and HGGDH. The model constants were defined to have an equivalent diffusion coefficient in case of isotropic turbulence, corresponding to $Sc_t = 0.5$ (section 3.2). The figure shows a very limited influence of the model, indicating that for the Reynolds stresses obtained from the k-ω SST model, the different formulations for the diffusion coefficient produce a similar result. Only in the region close to the wall the HGGDH model predicts higher scalar values.

5.2. *Sensitivity analysis*

In this initial sensitivity analysis, perturbations were introduced separately in the Reynolds stresses and the scalar fluxes, using the methodology outlined in section 4. The eigenvalues were perturbed by changing the location in the Barycentric map to one of the three corners (Figure 6) at all nodes. The turbulent kinetic energy was perturbed by multiplying or dividing the value obtained from the k-ω SST turbulence model by 2.

Figure 12 presents a comparison of the isolines obtained at the two most downstream locations either when perturbing the anisotropy of the Reynolds stress tensor toward the one-component corner of the Barycentric map or when modifying the turbulent kinetic energy by multiplying its value by 2. The left part of the figure shows the result when introducing the perturbations only in the Reynolds stress tensor in the momentum equation, hence showing the influence of the resulting modification in the mean flow on the scalar field; the right part shows the result when perturbing only the scalar flux vector in the scalar transport equation. The perturbation of the scalar flux vector also includes

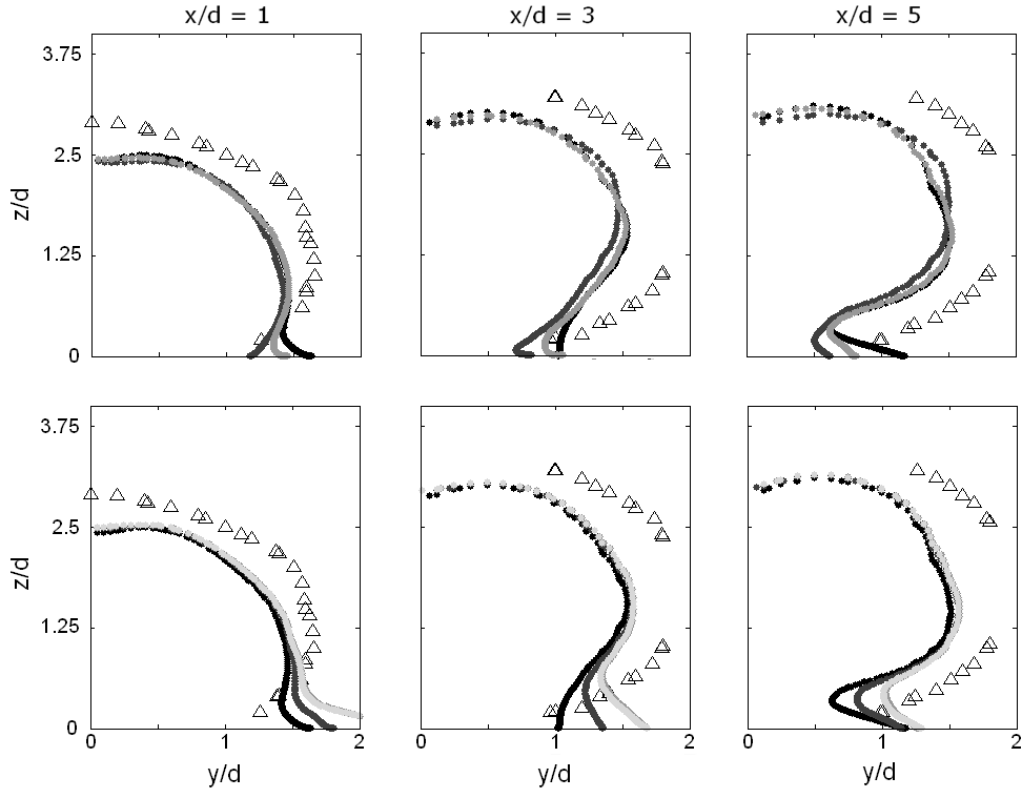

FIGURE 12. Isolines for $\phi = 0.028$ at two downstream transverse planes: LES (△), GGDH (•) and sensitivity of GGDH to $\Delta_{\lambda^{(i)}}$ (•) and Δ_k (•). Perturbations introduced separately in the Reynolds stress tensor in the momentum equations (top) and introduced in the GGDH model for the scalar flux vector in the scalar transport equation (bottom). A variation of Δ_{C_ϕ} (•) is also included (bottom).

the influence of multiplying the model constant by 2, which is equivalent to changing Sc_t in the SGDH model.

The results show that the isolines are sensitive to all perturbations introduced. It is worth noticing that the effect of the perturbations in the momentum equations is a decrease of the scalar values near the wall, whereas the perturbations of the scalar fluxes result in increased values. When perturbing the scalar fluzes, the influence of multiplying k by 2 and multiplying the model constant C_ϕ by 2 is almost identical, indicating that the diagonal terms of the scalar diffusion coefficient tensor largely determine the scalar flux vector. The preliminary EUQ study in the next section introduces all perturbations simultaneously.

5.3. *Preliminary EUQ study*

This preliminary study consisted of 16 simulations in which the parameters that determine the perturbation functions ($A1$ to $A4$ in Figure 10 and D and θ in Figure 8) were varied. Figure 13 presents the isolines for 4 simulations that are representative of the variability obtained. The baseline GGDH model result is shown, together with the perturbations that are obtained by using the peaks of the distributions for the parameters in the perturbations function. The two other cases included had both a different location

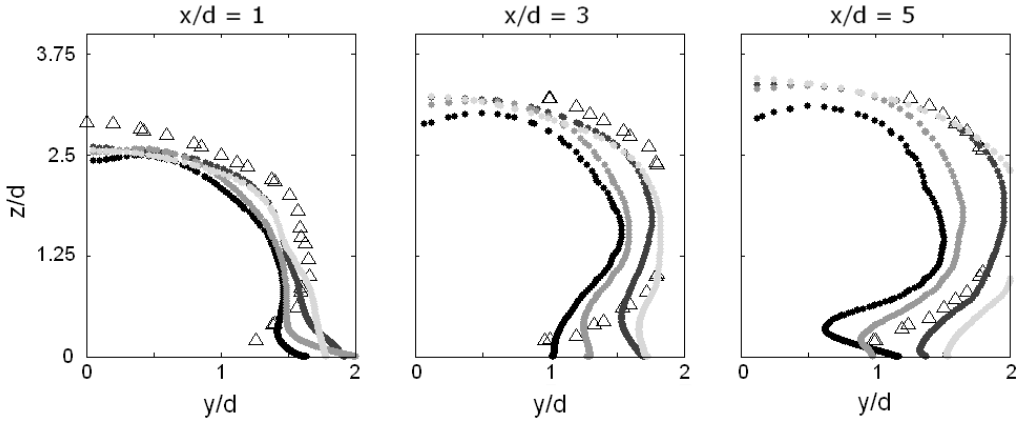

FIGURE 13. Variability in isolines for $\phi = 0.028$ obtained from preliminary EUQ study with the range of perturbations based on the LES/RANS comparison: LES (△), GGDH (●) and three different perturbations (●, ●, ●).

in the barycentric map and different amplitudes in the perturbation function for k. It is shown that even with this limited number of simulations, a relatively large variability is observed and at the most downstream location, the LES result is almost completely within the range of RANS solutions.

6. Conclusions and future work

The sources of uncertainty in RANS simulations of turbulent mixing are the Reynolds stresses in the momentum equations and the scalar fluxes in the scalar transport equations. To correctly quantify these uncertainties, perturbations are introduced in the values obtained from the models. The range of perturbations was determined based on a comparison with LES data. A preliminary EUQ study was performed, consisting of 16 simulations with varying perturbations. Despite the limited number of simulations, a significant variability is observed, demonstrating the potential of the approach.

Future work will include perturbing the eigenvectors of the anisotropy tensor and a comparison of the scalar fluxes obtained from the RANS mixing model (before and after introducing the perturbed Reynolds stresses) to the scalar fluxes available from the LES data set. The approach for specifying the perturbation functions will be further refined and a larger set of simulations will be run for a full EUQ study. Finally the methodology will also be applied to the configuration of Lin *et al.* (2010).

Acknowledgments

This material is based upon work supported by the Department of Energy [National Nuclear Security Administration] under Award Number NA28614.

REFERENCES

ABE, K. & SUGA, K. 2001 Towards the development of a Reynolds-averaged algebraic turbulent scalar flux model. *Int. J. Heat Fluid Flow* **22**, 19–29.

Banerjee, S., Krahl, R., Durst, F. & Zenger, C. 2007 Presentation of anisotropy properties of turbulence, invariants versus eigenvalue approaches. *J. Turb.* **8**, 1–27.

Ben-Yakar, A., Mungal, G. & Hanson, R. 2003 Time evolution and mixing characteristics of hydrogen and ethylene transverse jets in supersonic crossflows. *Phys. Fluids* **18** (2), 026101.

Boles, J., Edwards, J. & Baurle, R. 2010 Large-eddy/Reynolds-averaged Navier-Stokes simulations of sonic injection into Mach 2 crossflow. *AIAA J.* **48** (7), 1444–1456.

Daly, B. & Harlow, F. 2010 Transport equations in turbulence. *Phys. Fluids* **13**, 26342649.

Emory, M., Pecnik, R. & Iaccarino, G. 2011 Modeling structural uncertainties in Reynolds averaged computations of shock/boundary layer interactions. *AIAA Pap. 2011-0479* .

Gorlé, C. & Iaccarino, G. 2011 Large eddy and Reynolds-averaged Navier-Stokes simulations of an underexpanded sonic jet. In *7th Eur. Aerothermodynam. Symp.*.

Gruber, M., Nejad, A., Chen, T. & Dutton, J. 1995 Mixing and penetration studies of sonic jets in a Mach 2 freestream. *J. Propul. Power* **11** (2), 315–323.

Gruber, M., Nejad, A., Chen, T. & Dutton, J. 1997 Compressibility effects in supersonic transverse injection flowfields. *Phys. Fluids* **9** (5), 1448–1461.

Gruber, M., Nejad, A., Chen, T. & Dutton, J. 2000 Transverse injection from circular and elliptical nozzles into a supersonic crossflow. *J. Propul. Power* **16** (3), 449–457.

Gruber, M., Nejad, A. & Dutton, J. 1996 An experimental investigation of transverse injection from circular and elliptical nozzles into a supersonic crossflow. *Tech. Rep.* TR 96-2102. Wright Lab.

Kawai, S. & Lele, S. 2010 Large-eddy simulation of jet mixing in supersonic crossflows. *AIAA J.* **48** (9), 2063–2083.

Lin, K.-C., Ryan, M., Carter, C., Gruber, M. & Raffoul, C. 2010 Raman scattering measurements of gaseous ethylene jets in mach 2 supersonic crossflow. *J. Propul. Power* **26** (3), 503–513.

Pecnik, R., Terrapon, V. E., Ham, F. & Iaccarino, G. 2009 Full system scramjet simulation. *Ann. Res. Briefs 2009* pp. 33–45.

Santiago, J. & Dutton, J. 1997 Velocity measurements of a jet injected into a supersonic crossflow. *J. Propul. Power* **13** (2), 264–273.